ORIGINAL PAPER

Facile Hydrothermal Synthesis of Tungsten Tri-oxide/Titanium Di-oxide Nanohybrid Structures as Photocatalyst for Wastewater Treatment Application

Ujwala O. Bhagwat[1] · Karthik Raja Kumar[1] · Asad Syed[2] · Najat Marraiki[2] · Vinoth Kumar Ponnusamy[3,4,5] · Sambandam Anandan[1]

Abstract

In this study, tungsten trioxide/titanium dioxide (WO_3–TiO_2) nanohybrid structures were prepared using a facile hydrothermal method. The nanosheets-like morphology was achieved for the prepared WO_3–TiO_2 nanohybrid that were confirmed by scanning electron microscopy. Provided X-ray photoelectron spectroscopy results also confirm the element existence and surface composition of the nanohybrid structure. The optical properties of the WO_3–TiO_2 nanohybrid were verified using UV–Visible diffuse reflectance spectroscopy (UV–Vis DRS) and photoluminescence spectroscopy. The UV–Vis DRS results indicated that the absorption edge for the WO_3–TiO_2 nanohybrid found a red shift towards the visible region due to the reduced bandgap (2.83 eV). The photocatalytic activity of the as-prepared WO_3–TiO_2 nanohybrid was evaluated by the photocatalytic degradation of Orange G dye in wastewaters under visible light. 94% Orange G dye was degraded in 210 min at neutral pH in the presence of WO_3–TiO_2 nanohybrid, which indicates the enhanced photocatalytic activity. The photo-luminescence technique has also confirmed the formation of –OH radicals during photodegradation by utilizing terephthalic acid as a probe molecule. These results indicate that the prepared nanohybrid material is a simple, low-cost, and efficient photocatalyst for the degradation of pollutants in wastewater treatment applications.

Keywords WO_3–TiO_2 · Nanohybrid · Hydrothermal · Photocatalyst · Orange G · Photodegradation

Introduction

Recently, the use of semiconductor nanomaterials has received massive attention for the degradation of hazardous substances, namely organic dyes, heavy metal ions, microbes, pharmaceuticals, etc. released from the aqueous industrial outlet. Especially, hazardous dye solutions released from industries are the cause of water pollution. Azo dyes include over half of almost all of the dyes and colorants which are being used in industries on a large scale. Due to the rapid increase of industrialization, worldwide pollution control authorities want to solve the issues dealing with a vast amount of wastewater contaminated through dyes. For example, Orange G (azo dye) is the most harmful dye owing to its toxic and carcinogenic nature because of having auxochrome and –N=N– group in their chemical structure. The widespread use of Orange G in several domains leads to severe environmental issues caused by an evident and latent risk for living beings and

✉ Vinoth Kumar Ponnusamy
kumar@kmu.edu.tw

✉ Sambandam Anandan
sanand@nitt.edu

1 Nanomaterials and Solar Energy Conversion Lab, Department of Chemistry, National Institute of Technology, Tiruchirappalli 620 015, India

2 Department of Botany & Microbiology, College of Science, King Saud University, Riyadh 11451, Saudi Arabia

3 Department of Medicinal and Applied Chemistry & Research Center for Environmental Medicine, Kaohsiung Medical University, Kaohsiung City 807, Taiwan

4 Department of Medical Research, Kaohsiung Medical University Hospital (KMUH), Kaohsiung City 807, Taiwan

5 Department of Chemistry, National Sun Yat-Sen University (NSYSU), Kaohsiung City 804, Taiwan

the ecosystem [6, 41]. Advanced oxidation processes (AOPs) have focussed over the past four decades on destroying organic species, which are challenging to unadventurous techniques. AOPs generates continuously most reactive hydroxyl radicals upon using solar, chemical, or other forms of energy. The extremely reactive radical allows the degradation of a wide variety of organic species without selectivity is the most enticing feature of AOPs [24, 25].

The semiconductor nanomaterials show variable and controllable characteristics. The transition in energy structure and increased surface properties with reduced size have variable optoelectronic effects, in particular [17]. TiO_2 powder is a well-known photocatalyst commonly employed in several photocatalytic fields like the breaking down of organic contaminants, environmental purification, and photo splitting of water into H_2 (Hydrogen) and O_2 (Oxygen). Moreover, TiO_2 is a high-energy bandgap material that is 3.2 eV, and it can be excited only under UV irradiation (high energy) [9–12, 26]. Several UV-active oxides are customized to work as visible-light photocatalysts, by metal or anion doping. In general, these types of doped materials can only show a very small absorption in the visible region, which may lead to insignificant photocatalytic activities [3, 13].

Unlike single component photocatalysts, to evolve a visible light high-efficiency material, composite heterojunction of two semiconductor materials has been accepted as a tempting method. So, in recent years, to improve the photocatalytic properties of TiO_2, coupled semiconductors have been often proposed. Amongst, Tungsten trioxide (WO_3) coupling was performed to get better photocatalytic efficiency of TiO_2, since WO_3 acts as an electron-accepting species [20]. Besides, the photocatalyst WO_3 plays a significant role in energy and environmental problems to attain clean and recyclable hydrogen energy (i.e., WO_3 photocatalyst might be used as a potential electrode in water splitting). WO_3 nanocatalyst can absorb part of the visible light region (2.8–3 eV), and also it shows high resistance against photo corrosion in water solution [1, 19, 21, 28, 29]. However, WO_3/TiO_2 heterostructure nanomaterials were mostly synthesized by multi-step grafting of ammonium tungstate, physical mixing, coprecipitation method, sol–gel method, solvothermal crystallization, physical vapor deposition, etc. Normally these synthesis methods need to maintain temperature gradient and special types of equipment whereas such things are not required for the hydrothermal method.

In the present work, WO_3/TiO_2 heterostructures were prepared via a facile hydrothermal approach using titanium isopropoxide and sodium tungstate as precursors. Further, the photocatalytic efficiency of WO_3/TiO_2 heterostructures was examined for the degradation of Orange G dye under visible light illumination.

Experimental Section

Materials

Titanium isopropoxide, isopropyl alcohol, and sulphuric acid (H_2SO_4) were purchased from Alfa Aesar (India) and used without further purification. Sodium tungstate dihydrate ($Na_2WO_4 \cdot 2H_2O$) and Orange G were purchased from Sigma Aldrich (India). The other reagents used were of high purity (> 99%). In this work, all aqueous solutions were prepared using de-ionized water.
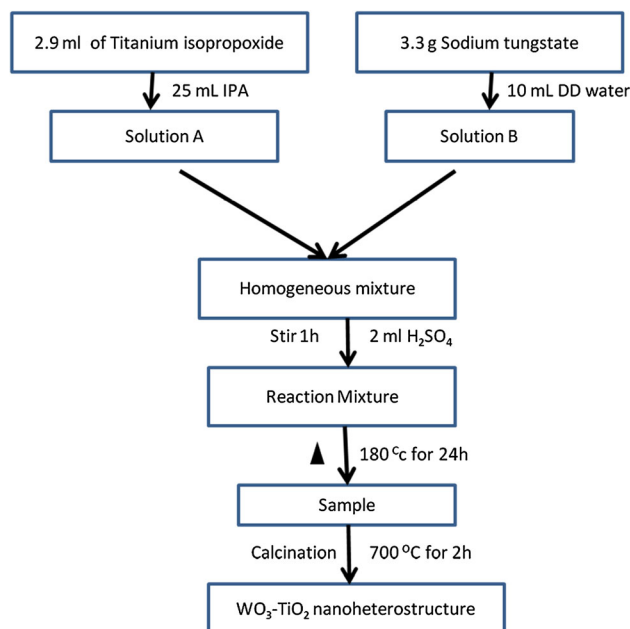
Synthesis of WO_3–TiO_2 Nanohybrid Structures

Titanium isopropoxide (2.9 mL) was first dispersed in 25 mL of isopropanol. To this solution, 10 mL of 1 M Sodium Tungstate solution was added and stirred well to get a homogenous solution. Then, added 2 mL of concentrated H_2SO_4 and stirred for 1 h. The obtained reaction mixture is safely transferred into a 100 mL autoclave and heated (180 °C) for 24 h in the vacuum oven by following the hydrothermal method. Afterward, the sample was washed, dried (100 °C), and then calcinated at 700 °C for 2 h to yield WO_3–TiO_2 nanoheterostructures. For comparison, samples were prepared by following similar procedures at different calcination temperatures, such as 500 °C and 600 °C. The schematic representation of the as-prepared material is shown in Fig. 1.

Characterization Analysis

Rigaku Ultima III X-ray diffractometer (XRD), Thermo Scientific Nicolet iS5 Fourier-Transform infrared (FTIR) spectrometer, JEOL Scanning Electron Microscope (SEM), and Transmission Electron Microscope (TEM) were used to analyze the as-prepared nanoheterostructure. The optical properties of the prepared material were studied in a Specord diode-array spectrophotometer and Shimadzu spectrofluorometer. A Shimadzu Total Organic Carbon (TOC) Analyzer was used to check the presence of organic carbon in the prepared nanohybrid material.

Photocatalytic Activity Studies

The photocatalytic experiments were performed in a photocatalytic reactor consisting of 150 W tungsten halogen lamp ($\lambda \geq 400$ nm; intensity $\approx 80,600 \pm 10$ lx). About 100 mL of Orange G dye solution in 3×10^{-5} M concentration with 75 mg of WO_3–TiO_2 nanoheterostructures

Fig. 1 Schematic representation of as prepared WO$_3$–TiO$_2$ nanohybrid structures

were taken in a 125 mL borosilicate glass bottle. The solution was kept stirring for 30 min under dark conditions to study the adsorption/desorption equilibrium by following the absorption of Orange G dye (λ_{max} = 480 nm). At regular time intervals, 4 mL of solution was taken from the mixture and filtered the catalyst by PVDF syringe filter (0.45 μm) then degradation of these dyes was studied using a UV–Vis spectrophotometer. The degradation kinetics were determined using (C/C$_o$) vs illumination time relationship. Importantly, no degradation was noticed without the catalyst.

Results and Discussion

The crystal structure of WO$_3$ is a three-dimensional arrangement of WO$_6$ octahedra in that W atoms are situated on the octahedra center, and oxygens are at the vertices. Hence, every oxygen forms a bond between W–O–W. The FTIR spectra of WO$_3$–TiO$_2$ nanoheterostructures (calcined at 500 °C, 600 °C, and 700 °C) are shown in Fig. 2a. It can be seen that the peak at 3609 cm^{-1} corresponds to the symmetry stretching vibration related to WO$_3$ and intercalated H$_2$O molecule and a low-frequency in-plane bending vibration observed at 1626 cm^{-1} corresponds to the W–OH plane. These vibrational features get reduced upon increasing the calcination temperature. Apart from these, a strong stretching frequency of W–O–W appears at 807 cm^{-1} for a 700 °C calcinated sample. This implies that the sample calcined at 700 °C is an optimum

temperature for the formation of WO$_3$–TiO$_2$ nanoheterostructures [33].

The powder XRD pattern of WO$_3$–TiO$_2$ nanoheterostructures calcined at 700 °C shown in Fig. 2b. The existence of the primary diffraction peaks of TiO$_2$ at θ = 25.28, 38.7, 40.0 were noticed, which might be indexed as (101), (004), (200) planes of anatase phase of TiO$_2$ (JCPDS card number 21-1272). The diffraction peaks corresponding to the WO$_3$ can be observed in the WO$_3$/TiO$_2$ nanoheterostructures at 2θ = 23.1, 23.7, 24.3, 26.6, 28.7, 33.3, 34.2, and 49.9 which might be assigned to (001), (020), (200), (120), (111), (021), (220), and (400) planes of the monoclinic phase of WO$_3$ (JCPDS card number 036-0101). Further, the powder XRD pattern of the sample calcined at 500 °C and 600 °C shows phase transformation of WO$_3$ (peaks are less intense) from amorphous to the crystalline monoclinic phase. Thus, it seems 700 °C be an optimized temperature for the calcination of WO$_3$–TiO$_2$ nanoheterostructures [14–16, 24, 25].

The chemical state of the present elements and surface composition in the WO$_3$–TiO$_2$ nanoheterostructure were studied by XPS. The XPS survey spectrum (Fig. 3a) shows the presence of Ti, W, and O species. In the W4f spectral region (Fig. 3b), the WO$_3$–TiO$_2$ nanoheterostructure displays a doublet at 35.63 and 37.59 eV matching with the W4f$_{7/2}$ and W4f$_{5/2}$ for chemical binding energy state. In the Ti2p plot, two distinctive peaks are observed at 458.9 and 461.2 eV belongs to the Ti2p$_{3/2}$ and Ti2p$_{1/2}$ energy levels of Ti^{4+} in WO$_3$–TiO$_2$ nanoheterostructure (Fig. 3c). In the spectral area of O1s (Fig. 3d), we noticed a broad and asymmetric peak at 530.5 eV, which may be attributed to WO$_3$–TiO$_2$ nanoheterostructure lattice oxygen [4, 23, 34].

The SEM image of WO$_3$/TiO$_2$ nanoheterostructure, looks-like nanosheets morphology (Fig. 4a, b). The provided TEM image (Fig. 4c, d) also supports such morphology. Figure 4e shows the HRTEM images of the as-prepared nanoheterostructure. The lattice spacing of 3.61 and 1.63 Å assigned to the monoclinic WO$_3$ (200) and (420) plane while the lattice spacing of 2.30 Å belongs to the (103) plane of anatase TiO$_2$, which also supports the formation of WO$_3$–TiO$_2$ nanoheterostructure. The selected area electron diffraction pattern (SAED) (Fig. 4f) shows that the crystallinity of WO$_3$–TiO$_2$ nanoheterostructure, which is inconsistent with the XRD patterns and besides this, the following crystal lattice planes (200), (103), and (420) matches well. The weight percentage of elements in the prepared sample was examined by EDS analysis indicates the availability of elements, namely, Ti, W, and O only (Fig. 4g). The weight % of WO$_3$–TiO$_2$ nanoheterostructure consists of W (58.08%), Ti (23.37%), and oxygen (18.55%).

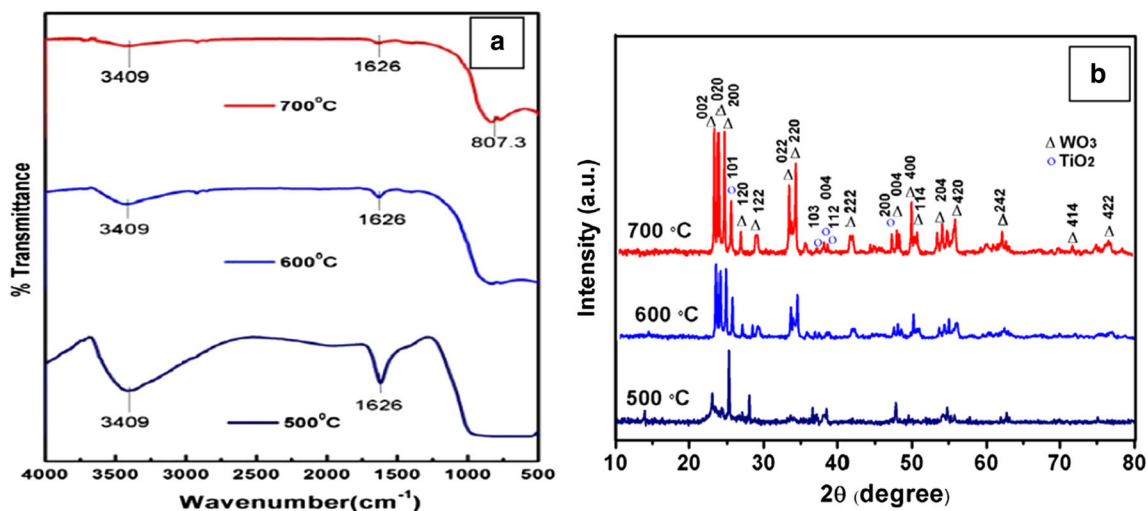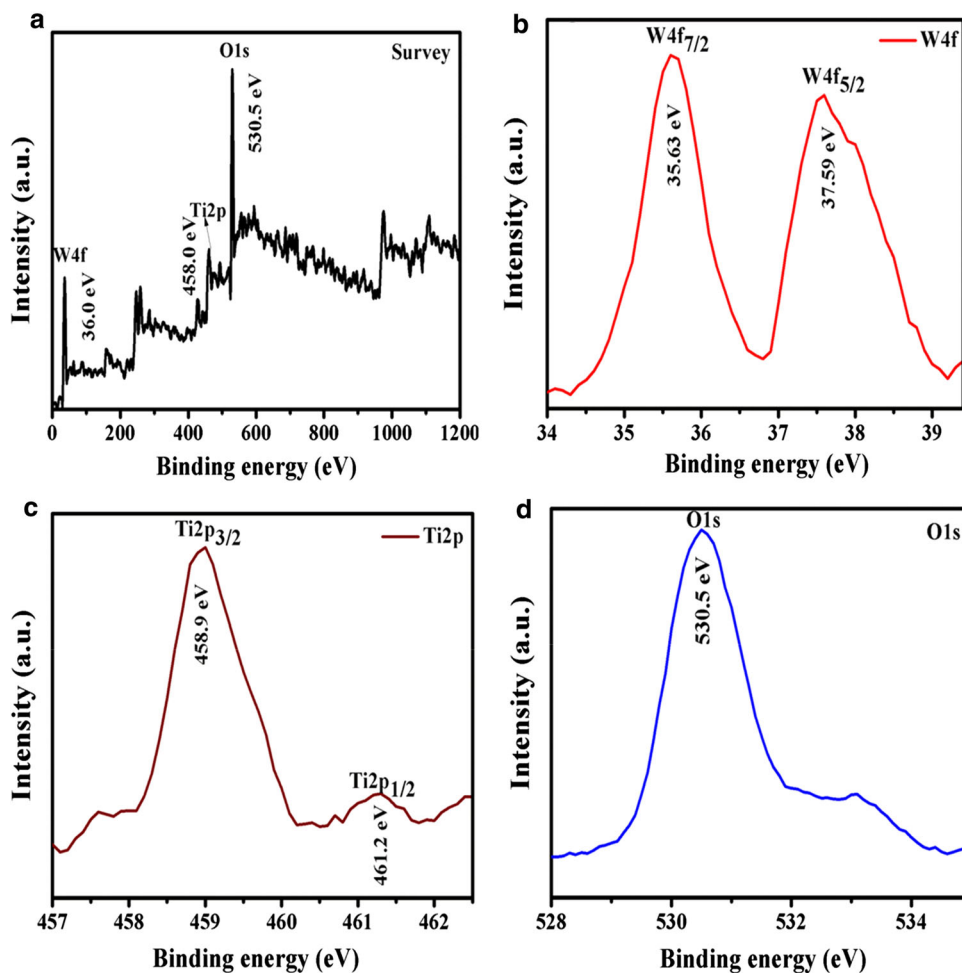The diffused reflectance spectra of the WO$_3$/TiO$_2$ nanoheterostructure calcined at 500 °C, 600 °C, 700 °C

Fig. 2 a FTIR spectra and **b** Powder XRD pattern of WO$_3$–TiO$_2$ nanoheterostructure at different calcination temperature

Fig. 3 XPS spectrum of WO$_3$–TiO$_2$ nanoheterostructure **a** Survey scan spectra, **b** W(4f), **c** Ti(2p). and **d** O(1s)


are shown in Fig. 5a. The absorption edge for the WO$_3$–TiO$_2$ nanoheterostructure was found red-shifted towards the visible region (475 nm) with an increase in the calcination temperature. Such absorption redshift is due to the occurrence of the defect energy levels in the forbidden band of TiO$_2$ and WO$_3$, which would reduce the bandgap [8, 18].

Fig. 4 **a**, **b** Low and High magnification FESEM images, **c**, **d** TEM images, **e** HRTEM image, **f** SAED pattern and **g** EDS spectrum of WO_3–TiO_2 nanoheterostructures
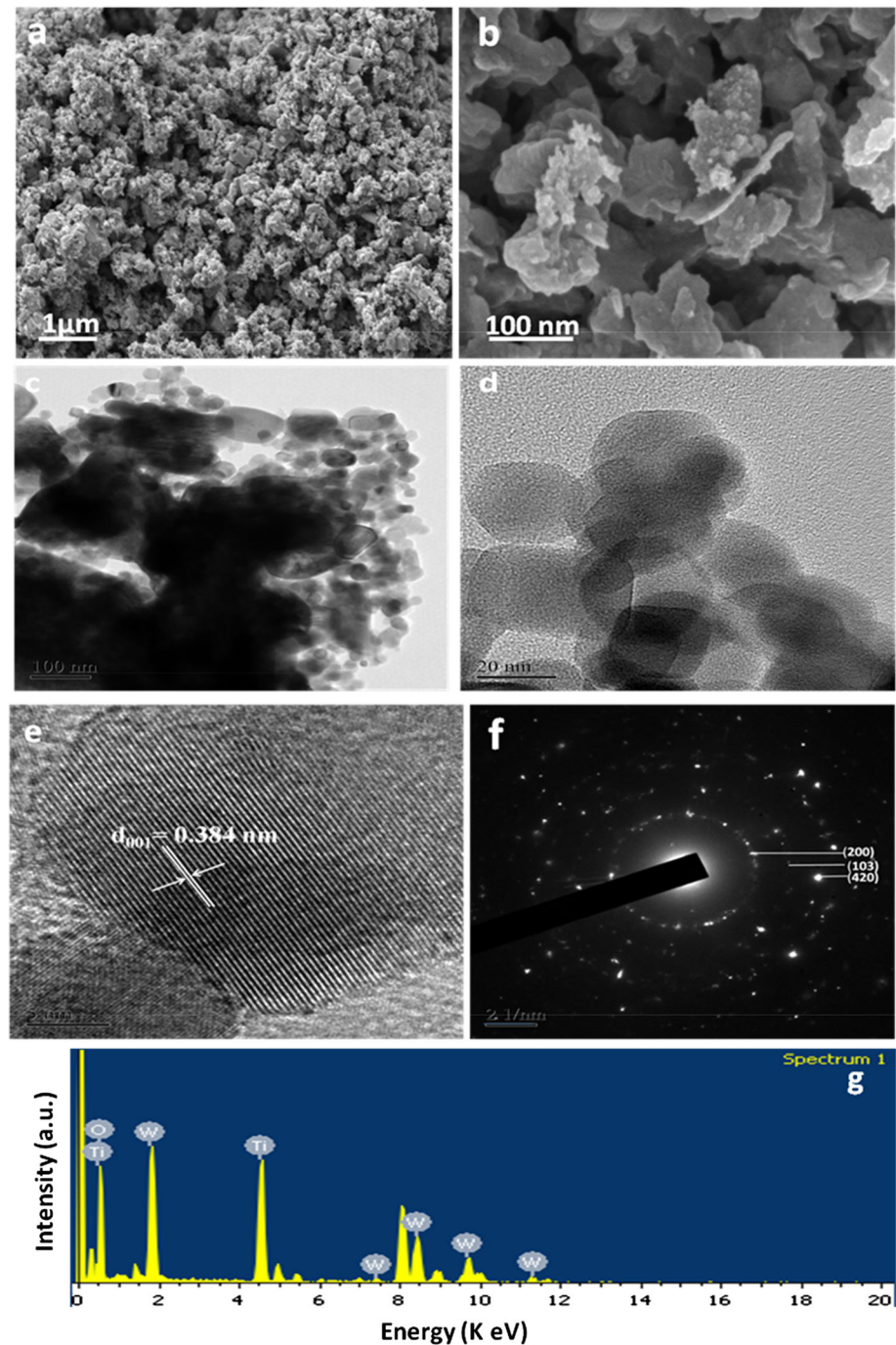

Using the Tauc plot approach, the bandgap for various WO_3–TiO_2 nanoheterostructures prepared at different calcination temperatures is calculated and shown in Fig. 5b. The extrapolated lines are used to evaluate the bandgap energies of as-prepared samples calcinated at different temperatures. The estimated bandgap of WO_3–TiO_2 nanoheterostructure calcined at 700 °C was found to be 2.83 eV, and its energy corresponds to the visible region.

The photoluminescence technique is used to analyze the effect of WO_3–TiO_2 nanoheterosturcture and the rate of the recombination of the electron–hole pairs. The photoluminescence spectra of WO_3–TiO_2 nanoheterostructure excited at 430 nm shows a strong emission peak at 469 nm (Fig. 5c). The PL intensity of WO_3–TiO_2 nanoheterostructure calcined at 700 °C is lower than 600 °C and 500 °C owing to the decrease in the radiative recombination process [5, 7].

The photocatalytic efficiency of the WO_3–TiO_2 nanoheterostructure (75 mg) was analyzed for the degradation of Orange G dye (3×10^{-5} M) under visible light.
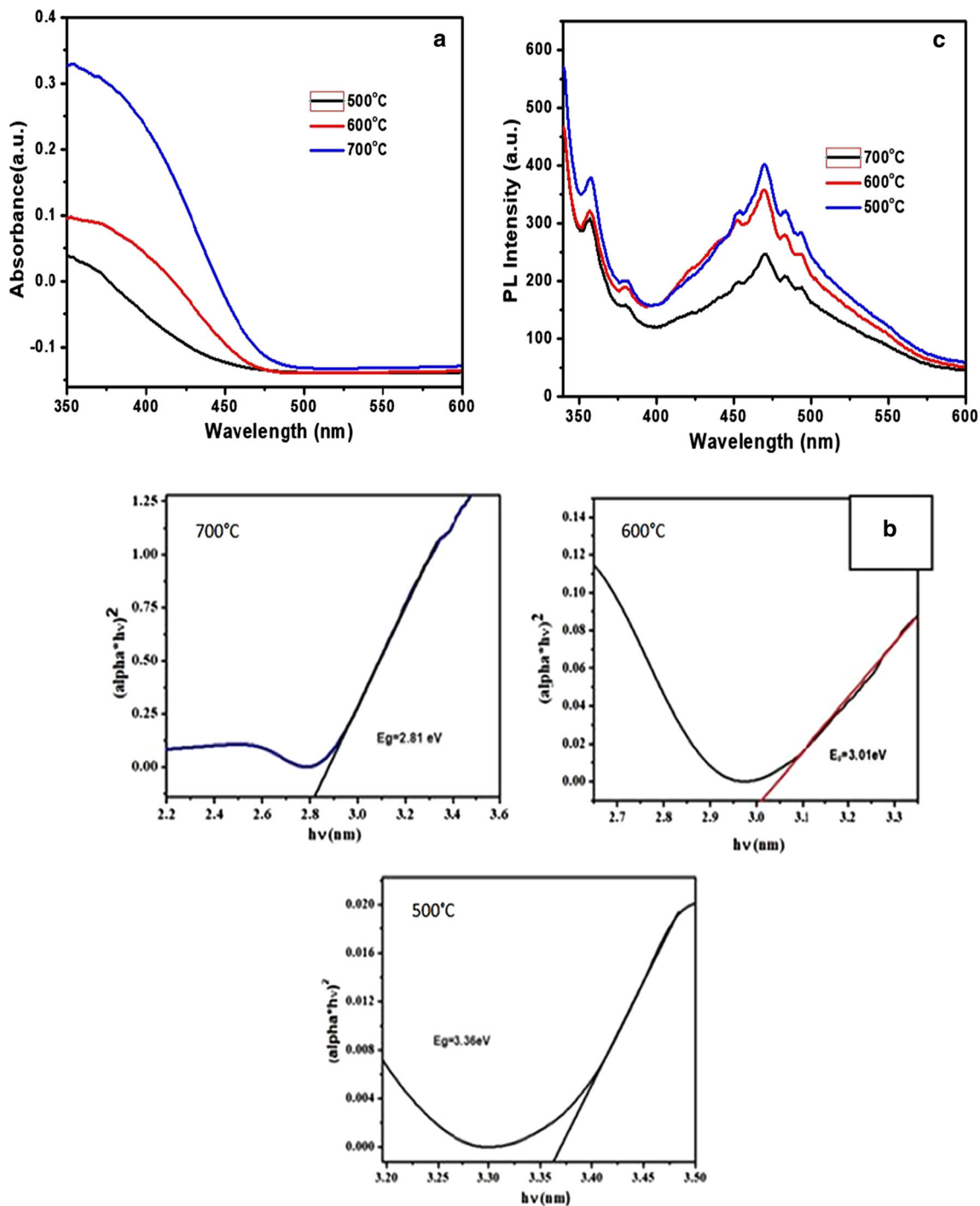
**Fig. 5** **a** UV–Vis diffuse reflectance spectra, **b** Tauc plot and **c** PL spectra of WO_3–TiO_2 nanoheterostructure

The UV–Vis absorption spectra of the Orange G solution at a regular time-period are shown in Fig. 6a. The absorption maximum at 480 nm belongs to the –N=N– chromophore group and other peaks attached to the naphthalene and benzene moiety [2, 27, 36–38]. The percentage calculation of dye degradation (D) was evaluated using the given formula,

$$\text{Percentage of dye degradation } (D) = \left(\frac{A_0 - A}{A_0}\right) \times 100\%$$

where A_o and A are the initial and the final concentration of Orange G solution.
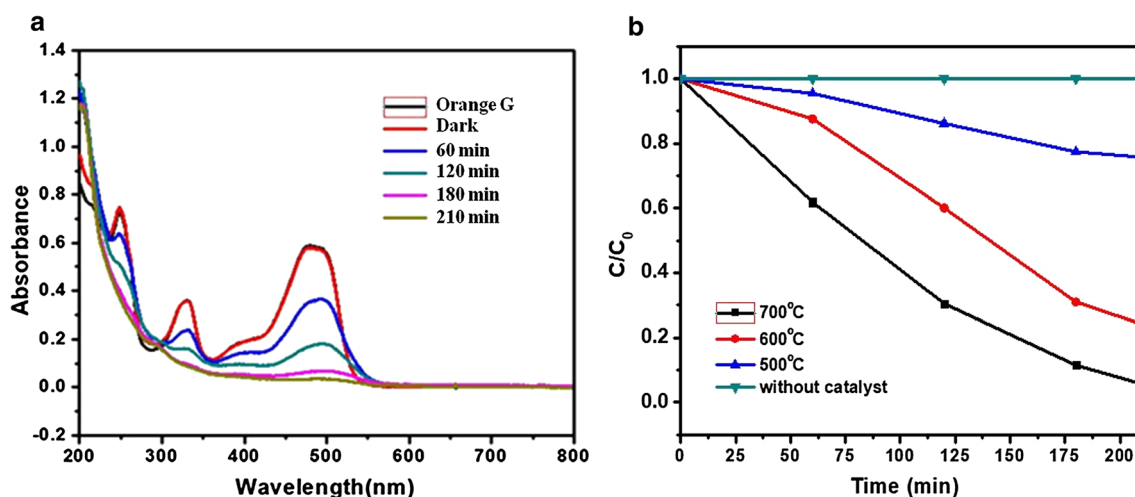
Fig. 6 a UV–Vis absorption spectrum of Orange G dye in the existence of WO_3–TiO_2 nanoheterostructure at different intervals of time during irradiation and **b** Photocatalytic degradation curve for WO_3–TiO_2 nanoheterostructure at different calcination temperatures in the presence of Orange G dye

The percentage of dye degradation is the efficiency of the photocatalyst and here the efficiency of prepared WO_3–TiO_2 nanoheterostructure reached 94% in 210 min.

Similar experiments were carried out using calcined material at 600 °C, 500 °C, and without a catalyst for comparison of the results (Fig. 6b). In the absence of a catalyst, there was no significant Orange G dye degradation. The degradation efficiency of Orange G calcined at 700 °C, 600 °C, and 500 °C were 94%, 75%, and 25% in 210 min. The WO_3–TiO_2 nanoheterostructure calcined at 700 °C shows superior photocatalytic activity that may be recognized to the bandgap position of the prepared material.

Figure 7a shows the effect of the catalyst amount (25–100 mg) for the photodegradation of Orange G dye (3×10^{-5} M). There is an increment in the percentage of Orange G degradation with an increase in the catalytic amount, and this is due to more active surface sites for the degradation processes [35, 40]. The optimized catalyst and dye concentration is 75 mg and (3×10^{-5} M).

The photocatalytic experiments were followed by varying the initial dye concentrations from (3–5) $\times 10^{-5}$ M by keeping the fixed photocatalyst quantity (75 mg) (Fig. 7b). The degradation efficiency decreases from 94 to 55% when the dye concentration increases from 3×10^{-5} to 5×10^{-5} M because light reaching the surface of photocatalyst decreases which in turn decreases the generation of active radicals [32].

During the photocatalytic processes, OH radicals are formed which is illustrated by performing experiments using terephthalic acid (TA) in the presence of WO_3–TiO_2 nanoheterostructures (Fig. 8). Hydroxy radical reacting with terephthalic acid produces 2-hydroxy terephthalic acid that shows fluorescence around 429 nm (λ_{ex} = 315 nm). Here, the fluorescence intensity was considerably increased, illustrate that OH radical is formed in the presence of WO_3–TiO_2 nanoheterostructure, and thus, the Orange G may be degraded [22, 30, 39].

To increase the photocatalytic efficiency further, photocatalytic degradation experiments were carried out with peroxomonosulfate (PMS; 0.3 mM) as an oxidant at a fixed

Fig. 7 Effect of **a** catalyst amount in mg and **b** and Initial dye concentration in Moles
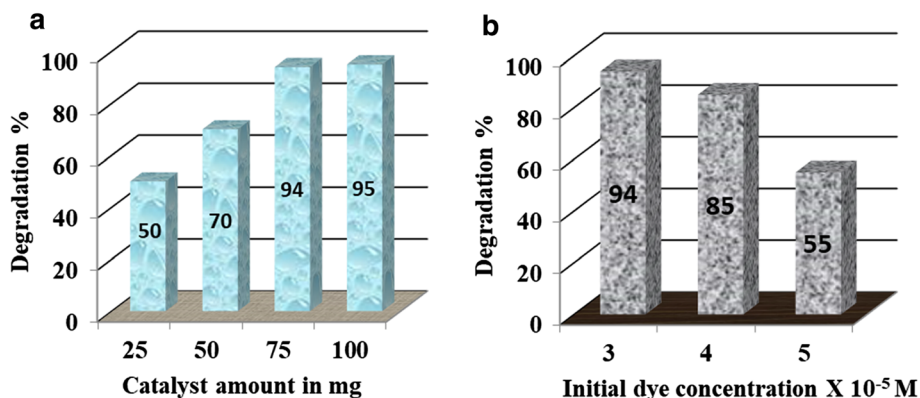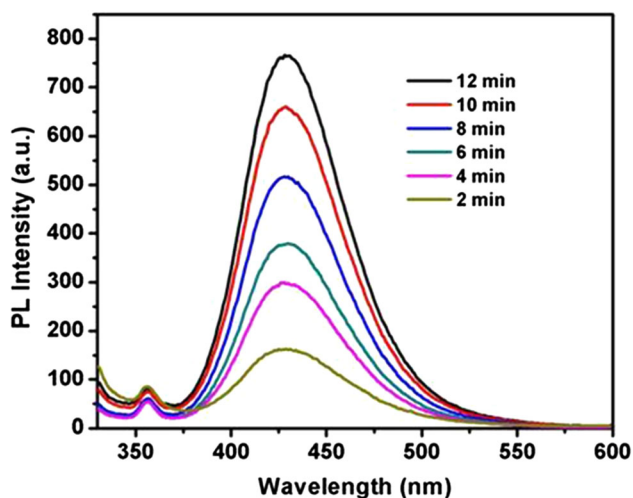
Fig. 8 PL spectra of Terephthalic acid in the presence of WO_3–TiO_2 nanoheterostructure under UV–Visible light irradiation

concentration of Orange G dye (3×10^{-5} M) and WO_3–TiO_2 nanoheterostructure (75 mg) (Fig. 9). The efficiency of photocatalytic degradation of dye was found to 97% in just 90 min in the presence of PMS while in the absence of oxidant noticed 94% degradation of dye in 210 min. Thus, the addition of oxidant causes an increase in the photocatalytic degradation rate due to the immediate trapping of photogenerated electrons by an oxidant, which eventually contributes to a decrease in the recombination rate of charge carriers, bringing more radicals. PMS is an effective oxidant and it is easily separated by the valence band holes and conduction band electrons of the WO_3–TiO_2 nanoheterostructure to generate more OH and SO_4 radicals [31].
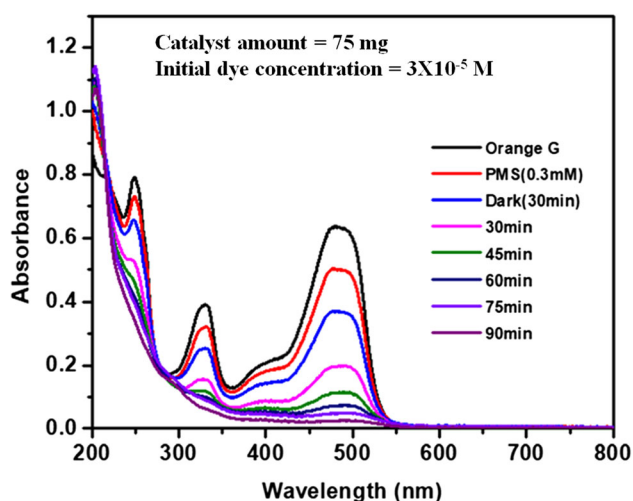
Fig. 9 Effect of PMS on the degradation of the Orange G in the presence of WO_3–TiO_2 nanoheterostructure under UV–Visible light irradiation

The photostability of WO_3–TiO_2 nanoheterostructure was established by collecting the photocatalyst sample after the experiment and a new photodegradation activity was carried out by utilizing the recyclable photocatalyst. Almost equivalent photocatalytic effectiveness after three repeated cycles demonstrates good stability (Fig. 10a). The stability of the recovered photocatalyst is confirmed by SEM analysis which illustrates no changes in the image after the photocatalytic experiment (Fig. 10b).

The mineralization of Orange G dye by WO_3–TiO_2 nanoheterostructure in an aqueous solution is determined through the total organic carbon (TOC) analysis. WO_3/TiO_2 exhibits 42.2% elimination of TOC in 210 min of the Orange G dye but it shows 94% efficiency for decolorization of the Orange G dye. This shows that the demineralization of the dye is slower compared to the decolorization (not fully mineralized). The TOC (%) was determined from the equation below

$$TOC(\%) = \frac{TOC_0 - TOC_t}{TOC_0} \times 100$$

where TOC_0 and TOC_t are the initial and final TOC concentrations, respectively.

Conclusion

In summary, we demonstrated the preparation and application of WO_3–TiO_2 nanohybrid structures towards photodegradation of Orange G dye. WO_3–TiO_2 nanoheterostructure has been synthesized via the hydrothermal method at different calcination temperatures. The XPS and EDX spectra confirmed the existence of W, O, and Ti only. The bandgap of as-synthesized WO_3–TiO_2 nanoheterostructure was 2.83 eV at a calcination temperature of 700 °C. The SEM image of WO_3–TiO_2 nanoheterostructure material confirms the nanosheet-like morphology. WO_3–TiO_2 nanoheterostructure material showed the lowest PL intensity at 700 °C calcination temperature and observed the highest photocatalytic activity while evaluated the other prepared samples at 500 °C and 600 °C calcination temperatures. The calculated mineralization of Orange G dye in aqueous solution by the total organic carbon (TOC) measurement is 42.2%. Therefore, the prepared WO_3–TiO_2 nanohybrid structured material can be a potential photocatalyst for the degradation of pollutants in wastewater treatment applications.
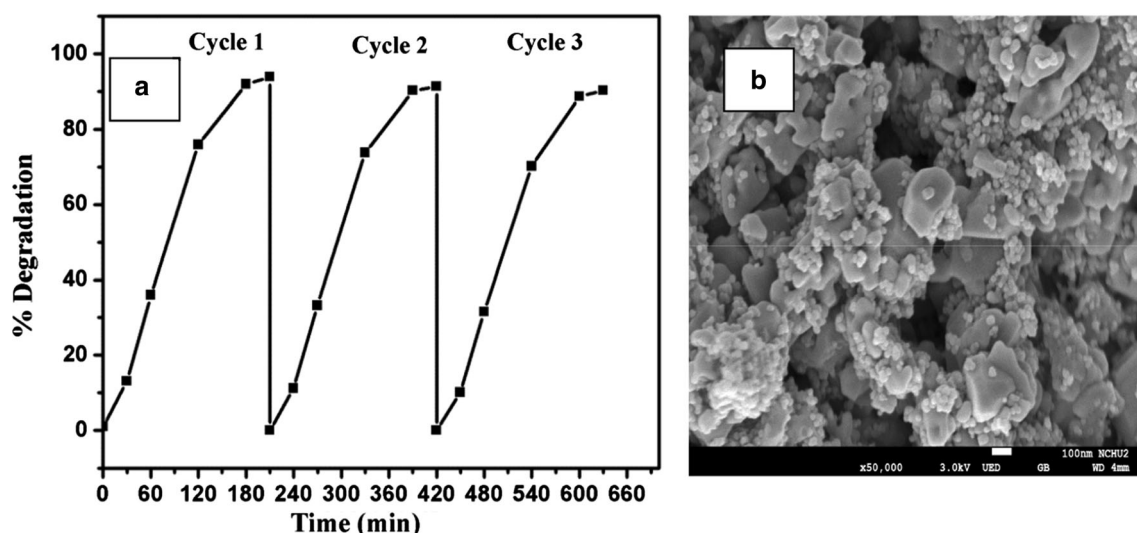
Fig. 10 **a** Photostability study of WO_3–TiO_2 nanoheterostructure for the photodegradation of Orange G dye solution and **b** SEM image of WO_3–TiO_2 nanoheterostructure after photocatalytic Orange G dye degradation

Author Contributions All the authors are equally contributed substantially to the work reported.

Data Availability All data generated or analyzed during this study are included in this published article.

Declarations

Conflict of interest The authors declare no conflict of interest.

References

1. S. Anandan and J. J. Wu (2014). Ultrasound-assisted synthesis of TiO_2–WO_3 heterostructures for the catalytic degradation of Tergitol (NP-9) in water. *Ultrason. Sonochem.* **21**, 1284–1288. https://doi.org/10.1016/j.ultsonch.2014.01.014.

2. A. Anshuman, S. S. Yarahmadi, and B. Vaidhyanathan (2018). Enhanced catalytic performance of reduced graphene oxide–TiO_2 hybrids for efficient water treatment using microwave irradiation. *RSC Adv.* **8**, 7709–7715. https://doi.org/10.1039/C8RA00031J.

3. M. A. Behnajady, B. Alizade, and N. Modirshahla (2011). Synthesis of Mg-doped TiO_2 nanoparticles under different conditions and its photocatalytic activity. *J. Photochem. Photobiol.* **87**, 1308–2131. https://doi.org/10.1111/j.1751-1097.2011.01002.x.

4. Y. P. Bhoi, S. R. Pradhan, C. Behera, and B. G. Mishra (2016). Visible light driven efficient photocatalytic degradation of Congo red dye catalyzed by hierarchical CuS-$Bi_2Cu_xW_{1-x}O_{6-2x}$ nanocomposite system. *RSC Adv.* **6**, 35589. https://doi.org/10.1039/C6RA02612E.

5. B. Boga, I. Székely, Z. Pap, L. Baia, and M. Baia (2018). Detailed spectroscopic and structural analysis of TiO_2/WO_3 composite semiconductors. *J Spectr.* https://doi.org/10.1155/2018/6260458.

6. D. Bokare, R. C. Chikate, C. V. Rode, and K. M. Paknikar (2008). Iron-nickel bimetallic nanoparticles for reductive degradation of azo dye Orange G in aqueous solution. *Appl. Catal. B* **79**, 270–278. https://doi.org/10.1016/j.apcatb.2007.10.033.

7. I. A. D. Castro and W. Ribeiro (2014). WO_3/TiO_2 heterostructures tailored by the oriented attachment mechanism: insights from their photocatalytic properties. *CrystEngComm* **16**, 1514–1524. https://doi.org/10.1039/C3CE41668B.

8. Z. Chen, J. Zhao, X. Yang, Q. Ye, K. Huang, C. Hou, Z. Zhao, J. You, and Y. Li (2016). Fabrication of TiO_2/WO_3 composite nanofibers by electrospinning and photocatalystic performance of the resultant fabrics. *Ind. Eng. Chem. Res.* **55**, 80–85. https://doi.org/10.1021/acs.iecr.5b03578.

9. P. Fitzpatrick and A. Ibhadon (2013). Heterogeneous photocatalysis: recent advances and applications. *Catalysts.* **3**, 189–218. https://doi.org/10.3390/catal3010189.

10. U. I. Gaya and A. H. Abdullah (2008). Heterogeneous photocatalytic degradation of organic contaminants over titanium dioxide: a review of fundamentals, progress and problems. *J. Photochem. Photobiol. C* **9**, 1–12. https://doi.org/10.1016/j.jphotochemrev.2007.12.003.

11. S. Girish Kumar and L. Gomathi Devi (2011). Reviews on modified TiO_2 photocatalysis under UV/visible light: selected results and related mechanisms on interfacial charge carrier transfer dynamics. *J. Phys. Chem. A* **115**, 13211–13241. https://doi.org/10.1021/jp204364a.

12. E. Grabowska, J. W. Sobczak, M. Gazda, and A. Zalesk (2012). Surface properties and visible light activity of W-TiO_2 photocatalysts prepared by surface impregnation and sol–gel method. *Appl. Catal. B* **117–118**, 351–359. https://doi.org/10.1016/j.apcatb.2012.02.003.

13. S. J. Hong, S. Lee, J. S. Jang, and J. S. Lee (2011). Heterojunction $BiVO_4$/WO_3 electrodes for enhanced photoactivity of water oxidation. *Energy Environ. Sci.* **4**, 1781–1787. https://doi.org/10.1039/C0EE00743A.

14. W. H. Hu, G. Q. Han, B. Dong, and C. G. Liu (2015). Facile synthesis of highly dispersed $WO_3·H_2O$ and WO_3 nanoplates for

electrocatalytic hydrogen evolution. *J Nanomater.* https://doi.org/10.1155/2015/346086.

15. B. Jin, E. Jung, M. Ma, S. Kim, K. Zhang, J. I. Kim, Y. Son, and J. H. Park (2018). Solution-processed yolk-shell-shaped WO₃/BiVO₄ heterojunction photoelectrode for efficient solar water splitting. *J. Mater. Chem. A* **6**, 2585–2592. https://doi.org/10.1039/C7TA08452H.

16. S. S. Kalanur, Y. J. Hwang, S. Y. Chae, and O. S. Joo (2013). Facile growth of aligned WO₃ nanorods on FTO substrate for enhanced photoanodic water oxidation activity. *J. Mater. Chem. A* **1**, 3479–3489. https://doi.org/10.1039/C3TA01175E.

17. P. Kanhere and Z. Chen (2014). A review on visible light active perovskite-based photocatalysts. *Molecules* **19**, 19995–20022. https://doi.org/10.3390/molecules191219995.

18. D. Ke, H. Liu, T. Peng, X. Liu, and K. Dai (2008). Materials Letters, Preparation and photocatalytic activity of WO₃/TiO₂ nanocomposite particles. *Mater. Lett.* **62**, 447–450. https://doi.org/10.1016/j.matlet.2007.05.060.

19. C. W. Lai (2018). WO₃-TiO₂ nanocomposite and its applications: a review. *Nano Hybrids Compos.* **20**, 1–26.

20. C. W. Lai and S. Sreekantan (2013). Discovery of WO₃/TiO₂ nanostructure transformation by controlling content of NH₄F to enhance photoelectrochemical response. *Adv. Mater. Res.* **620**, 173–178.

21. C. W. Lai and S. Sreekantan (2013). Fabrication of WO₃ nanostructures by anodization method for visible light driven water splitting and photodegradation of methyl orange. *Mater. Sci. Semicond. Process.* **16**, 303–310. https://doi.org/10.1016/j.mssp.2012.10.007.

22. G. Mendoza-Damián, F. Tzompantzi, R. PérezHernández, and A. Hernández-Gordillo (2016). Improved photocatalytic activity of SnO₂–ZnAl LDH prepared by one step Sn4+ incorporation. *Appl. Clay Sci.* **121–122**, 127–136. https://doi.org/10.1016/j.clay.2015.12.007.

23. Z. D. Mitrovi, S. Stojadinovi, L. Lozzi, S. Aškrabi, M. Rosi, N. Tomi, N. Paunovi, S. Azovi, M. G. Nikoli, and S. Santucci (2016). WO3/TiO2 composite coatings: structural, optical and photocatalytic properties. *Mater. Res. Bull.* **83**, 217–224. https://doi.org/10.1016/j.materresbull.2016.06.011.

24. D. Nagy, T. Firkala, E. Drotár, Á. Szegedi, K. László, and I. M. Szilágyi (2016). Photocatalytic WO₃/TiO₂ nanowires: WO₃ polymorphs influencing the atomic layer deposition of TiO₂. *RSC Adv.* **6**, 95369–95377. https://doi.org/10.1039/c6ra18899k.

25. M. Canle, M.I.F. Perez, and J.A. Santaballa (2017). Photocatalyzed degradation/abatement of endocrine disruptors. *Curr Opin Green Sustain Chem.* **6**, 101–138. https://doi.org/10.1016/j.cogsc.2017.06.008.

26. K. Nakataa and A. Fujishima (2012). TiO₂ photocatalysis: design and applications. *J Photochem. Photobiol C* **13**, 169–189. https://doi.org/10.1016/j.jphotochemrev.2012.06.001.

27. M. Y. Nassar, A. A. Ali, and A. S. Amin (2017). A facile Pechini sol–gel synthesis of TiO₂/Zn₂TiO₄/ZnO/C nanocomposite: an efficient catalyst for the photocatalytic degradation of Orange G textile dye. *RSC Adv.* **7**, 30411–30421. https://doi.org/10.1039/C7RA04899H.

28. B. Pal, B. L. Vijayan, S. G. Krishnan, M. Harilal, W. J. Basirun, A. Lowe, M. M. Yusoff, and R. Jose (2018). Hydrothermal syntheses of tungsten doped TiO₂ and TiO₂/WO₃ composite using metal oxide precursors for charge storage applications. *J. Alloys Compd.* **740**, 703–710. https://doi.org/10.1016/j.jallcom.2018.01.065.

29. C. Palanivel, N. R. Prabhakaran, and G. Selvakumar (2019). Morphological expedient flower-like nanostructures WO₃–TiO₂ nanocomposite material and its multi applications. *Open Nano* **4**, 100026. https://doi.org/10.1016/j.onano.2018.07.001.

30. J. Pan, X. Li, Q. Zhao, T. Li, M. Tade, and S. Liu (2015). Construction of MnO.5ZnO.5Fe₂O₄ modified TiO₂ nanotube array nanocomposite electrodes and their photoelectrocatalytic performance in the degradation of 2,4-DCP. *J. Mater. Chem. C* **3**, 6025–6034. https://doi.org/10.1039/C5TC01008J.

31. N. Pugazhenthiran, S. Murugesan, and S. Anandan (2013). High surface area Ag-TiO₂ nanotubes for solar/visible-light photocatalytic degradation of ceftiofur sodium. *J. Hazard. Mater.* **263**, 541–549. https://doi.org/10.1016/j.jhazmat.2013.10.011.

32. A. Rajini, M. Nookaraju, S. Chirra, A. K. Adepu, and N. Venkatathri (2015). Titanium aminophosphates: synthesis, characterization and Orange G dye degradation studies. *RSC Adv.* **5**, 106509–106518. https://doi.org/10.1039/C5RA19117C.

33. E. Safaei and S. Mohebbi (2016). Photocatalytic activity of nanohybrid CoTCPP@TiO₂/WO₃ in aerobic oxidation of alcohols under visible light. *J. Mater. Chem. A* **4**, 3933–3946. https://doi.org/10.1039/C5TA09357K.

34. S. M. F. Shaikh, S. S. Kalanur, R. S. Mane, and O. S. Joo (2013). Monoclinic WO₃ nanorods–rutile TiO₂ nanoparticles core–shell interface for efficient DSSCs. *Dalton Trans.* **42**, 10085–10088. https://doi.org/10.1039/C3DT50728A.

35. N. Tabatabaei, K. Dashtian, M. Ghaedi, M. M. Sabzehmeidani, and E. Ameri (2018). Novel visible light-driven Cu-based MOFs/Ag₂O composite photocatalysts with enhanced photocatalytic activity toward the degradation of orange G: their photocatalytic mechanism and optimization study. *New J. Chem.* **42**, 9720–9734. https://doi.org/10.1039/C7NJ03245E.

36. W. Wang, M. O. Tadé, and Z. Shao (2015). Research progress of perovskite materials in photocatalysis and photovoltaics related energy conversion and environmental treatment. *Chem. Soc. Rev.* **44**, 5371–5408. https://doi.org/10.1039/c5cs00113g.

37. Y. Wang, R. Priambodo, and H. Zhang (2015). Huang degradation of Azo Dye Orange G in fluidized bed reactor using iron oxide as a heterogeneous photo-Fenton catalyst. *RSC Adv.* **5**, 45276–45283. https://doi.org/10.1039/c5ra04238k.

38. C. L. Hsueh, Y. H. Huang, C. C. Wang, and C. Y. Chen (2006). Photooxidation of Azo Dye Reactive Black 5 Using a Novel-Supported Iron Oxide: Heterogeneous and Homogeneous Approach. *Water Sci Technol.* **53**, 195–201. https://doi.org/10.2166/wst.2006.197.

39. J. Zhang and Y. Nosaka (2013). Quantitative detection of OH radicals for investigating the reaction mechanism of various visible- light TiO₂ photocatalysts in aqueous suspension. *J. Phys. Chem. C* **117**, 1383–1391. https://doi.org/10.1021/jp3105166.

40. J. Zhang, M. Chen, and L. Zhu (2016). Activation of persulfate by Co₃O₄ nanoparticles for orange G degradation. *RSC Adv.* **6**, 758–768. https://doi.org/10.1039/C5RA22457H.

41. J. Zhu, Y. Koltypin, and A. Gedanken (2000). General sonochemical method for the preparation of nanophasic selenides: synthesis of ZnSe nanoparticles. *Chem. Mater.* **12**, 73–78. https://doi.org/10.1021/cm990380r.